Review

Latest Updates of Single-Junction Organic Solar Cells up to 20% Efficiency

Boudia Mohamed El Amine [1], Yi Zhou [2], Hongying Li [3], Qiuwang Wang [1], Jun Xi [4] and Cunlu Zhao [1,*]

[1] MOE Key Laboratory of Thermo-Fluid Science and Engineering, School of Energy and Power Engineering, Xi'an Jiaotong University, Xi'an 710049, China; amineboudia@stu.xjtu.edu.cn (B.M.E.A.)
[2] College of General Aviation and Flight, Nanjing University of Aeronautics and Astronautics, Nanjing 210016, China
[3] A*STAR Institute of High-Performance Computing, 1 Fusionopolis Way, Singapore 138632, Singapore
[4] MOE Key Laboratory for Physical Electronics and Devices & Shaanxi Key Lab of Information Photonic Technique, School of Electronic Science and Engineering, Xi'an Jiaotong University, Xi'an 710049, China
* Correspondence: mclzhao@xjtu.edu.cn

Abstract: Single-junction organic solar cells have reached a power conversion efficiency of 20% with narrow bandgap non-fullerene electron acceptor materials such as Y6, as well as with large band gap electron donor materials and their derivatives. The power conversion efficiency improvement of single-junction organic solar cells is a result of highly efficient light harvesting in the near-infrared light range and reduced energy losses with the most promising active layer layout currently available, Bulk-Heterojunction. Ternary blending is known to be the most advanced strategy to construct Bulk-Heterojunction structures in organic solar cells at present. In this review, we examine different devices based on Bulk-Heterojunction structures with efficient electron donors and acceptors. Then, we review the performance of binary and ternary organic solar cells with high power conversion efficiency, in conjunction with different anode and cathode interfaces used in recent studies of high-power conversion efficiency. Finally, we present perspectives on the future development of single-junction organic solar cells.

Keywords: organic solar cells; power conversion efficiency; bulk-heterojunction; ternary configuration

1. Introduction

Organic solar cells (OSCs) have emerged as a sustainable alternative to inorganic solar cell technology for power generation [1–7]. They can be fabricated using low-temperature solution processing and are widely considered to be an efficient type of solar energy harvesting device due to their low cost, short energy payback time, and mechanical flexibility [8–11]. Recently, single-junction OSCs (which use a single layer as an active layer) utilizing wide-band-gap polymer donors (PDs) and narrow-band-gap small-molecule acceptors (SMAs) as their bulk heterojunction (BHJ) photoactive layers have led to a power conversion efficiency (PCE) exceeding 18% [12]. In most organic materials, the short exciton diffusion length, which is typically only a few nanometers, is a critically limiting factor for achieving high efficiency OSCs. BHJ exhibiting nanoscale phase separation between the donor-acceptor (D-A) mixture has been recognized for its ability to overcome the limitation of short exciton diffusion lengths [13]. Another factor that affects the PCE and stability of OSCs is the morphology of the solution-processed active layer, which is difficult to control [13–17]. The PCE, together with the devices' durability and lifespan, are the most significant problems attributed to OSCs that hinder large-scale applications. Recent advances in OSCs include the following: the use of new non-fullerene SMAs with high light absorption, reduced loss in the driving force for charge separation, improved film morphology, the use of novel interfacial layers in device engineering, etc. [18,19].

Recent investigations of single-junction OSCs with high efficiency are summarized in Table 1. In 2019, Yao et al. [20] synthesized a non-fullerene acceptor (NFA) called BTP-4Cl-12 to fabricate spin-coated OSCs within a small area (~0.09 cm^2). They adopted a device structure of ITO/PEDOT: PSS/PM6: BTP-4Cl-12/PDINO/Al (ITO: indium tin oxide; PEDOT: PSS: poly (3,4-ethylene dioxythiophene): poly-(styrene sulfonate); PDINO: (perylene diimide functionalized with amino N-oxide), leading to a high PCE of 17% (16.6% as the certified value). In 2020, an active layer consisting of a mixture of the mid-band gap donor PM6 and the low-band-gap NFA Y6 showed an exceptional PCE of ~16%, a short-circuit current density (J_{sc}) of ~25 mA cm^{-2} and a low energy loss (E_loss) of 0.5–0.6 eV [21]. Zhang et al. [22] achieved a high PCE of 17.23% using the structure of an ITO/PEDOT: PSS/PM6:Y6/PDINN/electrode. Their study used a highly conductive cathode interface of PDINN instead of PDINO. This modification dramatically impacts the electron transport and exciton diffusion at the cathode interface and also results in better contact between the non-fullerene electron acceptor and the metal electrode. In 2021, single-junction OSC cells attained a PCE of 19.0% (certified value: 18.7%) via an active layer material design with a ternary mixing technique. Namely, the mixture of a wide-bandgap polymer donor called PBQx-TF, and a low-bandgap NFA eC9-2Cl. A second NFA named F-BTA3 serves as a third component on the active layer [23]. Finally, Ram and Singh [24] studied the ternary organic solar cell (TOSC) with the structure of moth-eye-AR/glass/ITO/WS2/PBDB-T-2F: Y6: SF(BR)4/PFN-Br/Al and showed that the TOSC achieved a theoretical PCE of 20.87%, which is the highest among OSCs at present. Such a high PCE can be attributed to the tungsten disulfide (WS2) hole transport layer (HTL), which minimized the contact resistance between the active layer and the anode, leading to a high internal quantum efficiency of 91.7%. The ternary structure in OSCs can improve the stability of the device and the charge transport between the active layers. The addition of a third component to the active layer has improved the efficiency of charge extraction by the electrodes and reduced internal resistance. These highly encouraging results show great promise for large-scale production and commercialization of OSCs in the next few years.

Table 1. A summary of recent studies of single-junction OSCs with high efficiency.

Active Layer	Anode Layer	Cathode Layer	J_{sc} (mA cm^{-2})	V_{oc} (V)	FF (%)	PCE (%)	Year	Ref.
PM6:BTP-4Cl-12	PP	PDINO	25.60	0.858	77.60	17.00	2019	[20]
PM6:Y6	PP	PDINN	25.89	0.847	78.59	17.23	2020	[22]
PBQ6:Y6	PP	PDINN	26.58	0.851	77.91	17.62	2021	[25]
PM6:BTP-eC9	PP	PFN-Br	26.20	0.841	78.30	17.80	2020	[26]
D18:Y6	PP	PDINN	27.70	0.859	76.60	18.22	2020	[27]
PBDB-T-2F:Y6:PC71BM	WS2	PFN-Br	26.00	0.840	78.00	17.00	2019	[28]
PM6:Y6:C8-DTC	PP	PDINO	26.50	0.873	75.61	17.52	2020	[29]
PM6:BTP-eC9:PC71BM	PP	PFN-Br	26.93	0.856	79.40	18.30	2020	[30]
PBQx-TF:eC9-2Cl:F-BTA3	PP	PNDIT-F3N-Br	26.7	0.879	80.90	19.0	2021	[23]
PBDB-T-2F:Y6:SF(BR)4	WS2	PFN-Br	29.31	0.89	80	20.87	2020	[24]

In this review, we examine different BHJ-based OSC devices with efficient electron donors and acceptors, comparing the performance of binary and ternary OSCs. Next, we discuss different anode and cathode interfaces used in recent OSCs with high PCE. Finally, we propose solutions to problems that hinder the commercialization of OSC technology using results obtained from this study that demonstrate better-designed device structures with binary and ternary BHJ.

2. Device Architecture and Working Principles

Significant progress has been made for single-junction OSCs in recent years. Most of the research has been dedicated to developing novel materials with increased charge carrier mobility and improved light absorption properties [31]. Figure 1a presents binary

OSCs schematically with single junction BHJ architecture, and Figure 1b depicts the energy level diagram corresponding to the OSC in Figure 1a. As the active layer of the polymer cell absorbs the photon of incident light by either donor or acceptor, the highest occupied molecular orbital (HOMO) of the donor and acceptor materials is stimulated to its lowest unoccupied molecular orbital (LUMO), and simultaneously electron-hole pairs called excitons form in the active layer [32–34]. The excitons diffuse across the donor and acceptor phases, and then become dissociated at the interface between the donor and acceptor. The exciton dissociation consists of two steps: First, when an exciton excited in the donor reaches the D-A interface, the electron is transferred to the acceptor's LUMO. At the same time, when an exciton excited in the acceptor reaches the D-A interface, the hole is transferred to the donor's HOMO, which is at a lower energy level. In the second stage, the exciton will dissociate if the energy offset is at least equivalent to the exciton's binding energy [33]. The dissociated electron is transported through the acceptor phase via its LUMO, and across the interface between the acceptor and the cathode. The dissociated hole is transported through the donor phase via its HOMO, collected at the HTL, and simultaneously transferred to the anode. The energy offsets are considered the driving force for charge transfer between organic molecules in the OSCs. The energy offset equal to the HOMO offset of the donor and acceptor ($\Delta E = E^{D}_{HOMO} - E^{A}_{HOMO}$) is released as molecular vibrational energy [33]. If $\Delta E \geq E_{B}$ (wherein E_{B} is the exciton binding energy), the released molecule vibrational energy may separate the excitons into free electrons and holes, which are collected at the anode/cathode and may thus contribute to the photovoltaic current [33]. Consequently, decreasing these energy offsets has an immediate effect on the open-circuit voltage (V_{oc}) of the solar cell and, accordingly, its PCE. When light is absorbed by the acceptor molecule, a similar charge transfer process occurs, except that the exciton dissociation is prompted by the favorable transfer of a hole from the acceptor's HOMO to the donor's HOMO.
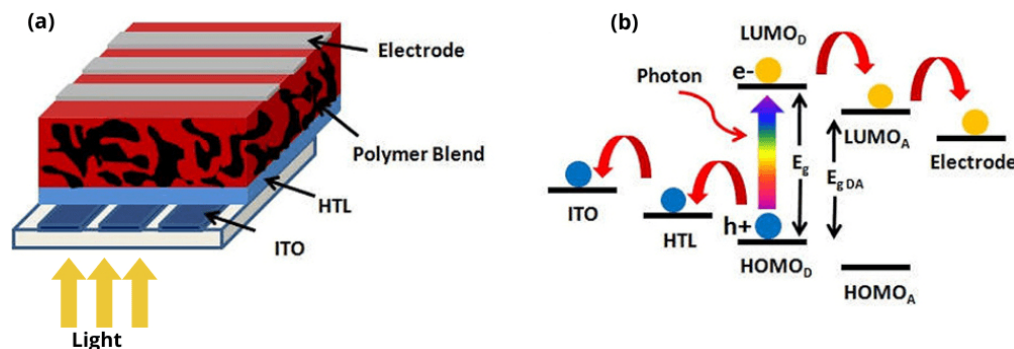

Figure 1. (**a**) Single junction BHJ architecture with a blend of polymer donor (red) and acceptor (dark) materials as the active layer. (**b**) Schematic of charge (hole and electron) transport in a single junction BHJ cell (Reprint with permission from Ref. [32]. 2023, Frontiers).

The relationship between electric current density and external voltage (known as *J-V* curves) characterizes the electrical performance of a photovoltaic cell. Figure 2a shows typical *J-V* curves for a solar cell under darkness (dashed lines) and illumination (solid lines) [26]. The *J-V* curves under darkness and illumination can be predicted from Shockley's equations as

$$J(V) = J_0 \left[exp\left(\frac{eV}{nkT} \right) - 1 \right] \text{ (under darkness)} \tag{1}$$

$$J(V) = J_0 \left[exp\left(\frac{eV}{nkT} \right) - 1 \right] + J_{ph} \text{ (under illumination)} \tag{2}$$

where the first equation describes the *J-V* characteristics under darkness and the second equation describes *J-V* characteristics under illumination; J_0 is the reverse dark current and

V is the voltage, e is the electron charge, n is the diode quality factor, k is the Boltzmann constant, T is the temperature, and J_{ph} represents the light-induced current.
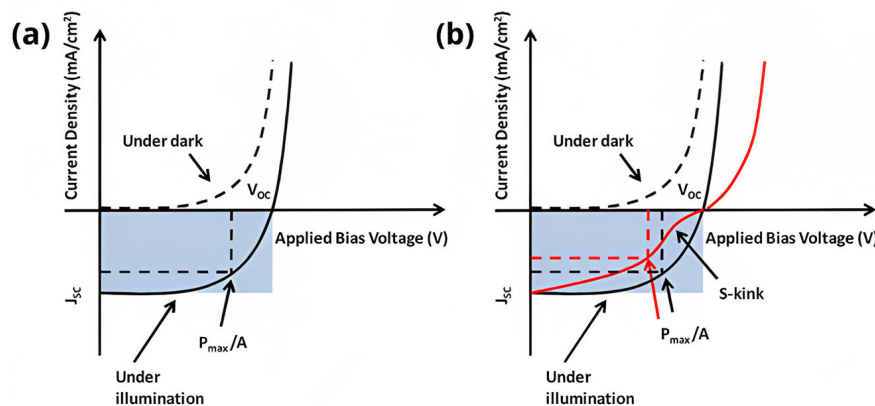

Figure 2. (**a**) *J-V* curves of a solar cell under darkness and light, as well as the corresponding photovoltaic characteristics; (**b**) *J-V* curves with the "S-kink" feature (Reprint with permission from Ref. [32]. 2023, Frontiers).

Figure 2a depicts the performance characteristics of solar cells, including the short-circuit current density (J_{sc}), the open-circuit voltage (V_{oc}), and the maximum operational power (P_{max}) that determines the fill factor (*FF*). V_{oc} is the maximal voltage that corresponds to zero current in the solar cell, while the short-circuit current density represents the maximal current density that corresponds to zero voltage across the solar cell. *FF* is defined as the ratio of P_{max} to the maximum power extractable from an ideal solar cell (evaluated as a product of the device area (A), V_{oc} and J_{sc}). The PCE (η) is the ratio of the solar cell's maximum operational power to the incident light's input power. Therefore, for an incident light intensity of I_{in}, *FF* and PCE (η) can be expressed as [8,25,27–30,35–41]:

$$FF = \frac{P_{max}}{A J_{sc} V_{oc}} \tag{3}$$

$$\eta = \frac{J_{sc} V_{oc}}{I_{in}} \tag{4}$$

The *FF* has a direct correlation with the efficiency of charge extraction in OSCs. Low *FF* indicates a larger loss of charge carriers due to molecular recombination at the donor-acceptor interface and the intermediary layers interfaces in BHJ OSCs [8].

One key factor contributing to the improved performance of organic solar cells is the efficient transfer of charge across various interfaces within the device. The type and quality of the interfaces between the layers of a solar cell affect the charge transfer across the interfaces and, hence, the PCE and FF. Due to poor interfacial conditions, many practical organic BHJ devices show the "S-kink" feature in the *J-V* characteristics (see Figure 2b), indicating the reduction of FF and PCE within the BHJ solar cell. In addition to interfacial properties, oxygen doping, the presence of organic contaminants, vertical phase segregation, low surface recombination, and the creation of charge dipoles all contribute to the development of the "S-kink." When producing high-quality BHJ solar cells, it is essential to perform comprehensive characterization to have proper control over crucial physical characteristics, such as layer thickness, interfacial conditions, and morphology. The morphologies of thin film materials can change over time at room temperature during operation, and thus morphologies of materials in different layers of the solar cell gradually become unstable as they naturally degrade. These morphological changes in the active layer are dependent on the fabrication process [26,42,43].

There are more advanced configurations of OSCs beyond the conventional configuration shown in Figure 2a, such as the ternary configuration shown in Figure 3. Figure 3a presents the film absorption spectra of the three active materials of ternary OSCs, namely,

donor 1(D1), donor 2 (D2), and acceptor (A)). Ternary solar cells made up of donor 1 (D1), donor 2 (D2), and acceptor (A) exhibit the benefits of a straightforward device design (Figure 3b) and a broad range for photon capturing. Unlike the traditional binary solar cells, the mechanism behind the photovoltaic process in ternary solar cells is not simply a combination of the photovoltaic processes of individual cells. Three key concepts play roles in ternary solar cells: charge transfer, energy transfer, and parallel-linkage or alloy structure, which are greatly impacted by the presence of the third component (either the second donor or acceptor) in the ternary active layer [35]. The third component in the ternary system can be integrated within the donor, fully incorporated in the acceptor, situated at the interface between the donor and acceptor, or create its own pathways (as shown in Figure 3b).
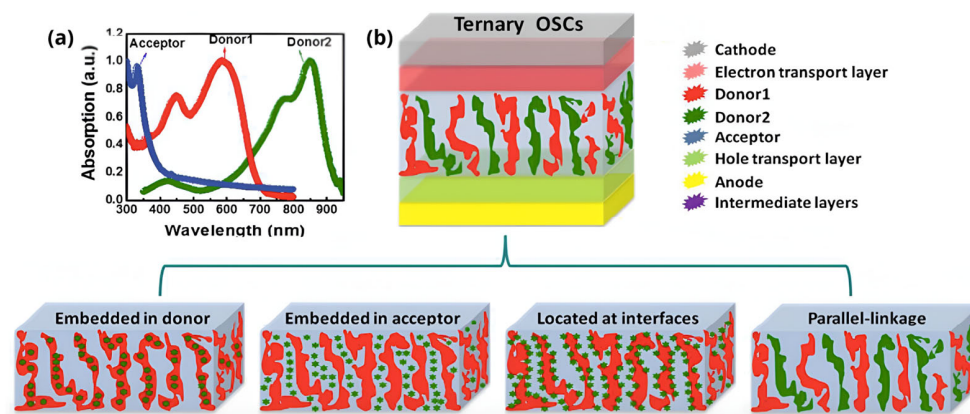

Figure 3. The schematic configuration of a ternary OSCs: (**a**) Film absorption spectra of three active materials; (**b**) Ternary BHJ architecture with four potential active layer morphologies based on the placement of the third component. (Reprint with permission from [35]. 2023, Royal Society of Chemistry).

2.1. Binary OSC Structure

The use of NFAs in OSCs has led to a PCE as high as 18% [26,29,30,35,36]. In 2019, Yao et al. [20] used a highly efficient NFA BTP-4Cl in the active layer of the OSCs and studied the performance of the OSC materials under different processing conditions. Impressively, the device with PBDB-TF: BTP-4Cl-12 as the active layer materials achieved a PCE of 17.0% for an active layer area of 0.09 cm^2. The same team published another study in 2020 with the same processing conditions and active layer structure [25]. The study shows that the single-junction OSCs with BTP-eC9 (only modifying the electron acceptor) extracted from Y6 (BTP-4F) by modification of alkyl chains has achieved a PCE of 17.8%. These results show the importance of the alkyl chain modification in light absorption and power conversion. The authors hypothesized that by further improving donor materials or device engineering with multiple-compound mixing and morphological control, a greater PCE may be attained. A comparison of the photovoltaic performance of the two studies shows that the use of NAF BTP-eC9 leads to V_{oc} = 0.839 V, J_{sc} = 26.2 mA cm^{-2} and *FF* = 0.811 [25], and the other use of BTP-4Cl-12 produces V_{oc} = 0.858 V, J_{sc} = 25.6 mA cm^{-2} and *FF* = 0.776 [20]. Typically, the PCE for a PBDB-TF: BTP-4Cl-12 structure is lower than that of a PBDB-TF: BTP-eC9 structure due to low J_{sc} and *FF* values. To investigate the cause of the enhancement of BTP-eC9 based OSCs, Yao et al. [20] conducted photoinduced charge carrier extraction in linearly increasing voltage (photo-CELIV) measurements to characterize the mobility of the charge carriers in the working OSCs. The charge carrier (electrons) mobilities are determined to be 2.78×10^{-4} and 2.92×10^{-5} cm^2 V^{-1} s^{-1} for the devices based on BTP-eC9 and BTP-4Cl-12, respectively. Then, they varied the light intensity (P_{light}) from 1 to 100 mW cm^{-2} and analyzed the impact of the P_{light} on the photovoltaic parameters (J_{sc} and V_{oc}). The slope (S′) of ΔV_{oc} versus $\Delta \ln (P_{light})$, is acknowledged as a strong indicator of trap-state-assisted charge recombination. The calculated S′ values are 1.04 and 1.19 $kT\,e^{-1}$ for BTP-eC9 and BTP-4Cl-12 based devices, respectively, under

the same processing conditions. The low S′ value of the BTP-eC9-based device implies that trap-assisted recombination is suppressed in the device. The significantly increased S′ value of BTP-4Cl-12 is one of the main reasons for its decreased PCE. The results show that a PBDB-TF: BTP-eC9 based device has less charge carrier recombination, which contributes to the high PCE. To understand the reasons for these results more thoroughly, they performed morphology characterization of the active layer films using atomic force microscopy (AFM). The surface roughness is 1.34 nm and 7.92 nm for PBDB-TF: BTP-eC9 and PBDB-TF: BTP-4Cl-12 devices, respectively, indicating a large difference between the two devices. The first structure has proper crystallinity, high solubility, and aggregation properties, while the second does not. High solubility and aggregation properties can significantly improve the morphology of the acceptor/donor blend, thereby enhancing the crystallinity inside the material and the PCE of the device. In 2020, Ma et al. [29] produced a binary BHJ device based on PM6: Y6 (1:1.2, *w/w*), giving rise to a PCE of 16.20% with a V_{oc} of 0.846 V, a J_{sc} of 25.6 mA cm^{-2} and an FF of 73.88%. The PM6:C8-DTC (1:1.2, *w/w*) based binary device has a lower PCE of 12.06%, a higher V_{oc} of 0.952 V, a lower J_{sc} of 16.87 mA cm^{-2}, and a higher FF of 75.03% [29]. Materials such as PM6, PBQ6, D18, and PBDB-T-2F are some of the most commonly used electron donors that have been developed and studied in the past decade. In 2020, Liu et al. [27] disclosed a polymer donor called D18 using a fused-ring acceptor unit, i.e., dithieno [3′,2′:3,4;2″,3″:5,6] benzo[1,2-c][1,2,5] thiadiazole (DTBT), and found that the D18: Y6 BHJ structure solar cells achieved a PCE of 18.22% (certified 17.6%). Solar cells in this study have a structure of ITO/PEDOT: PSS/D18: Y6/PDINN/Ag. The active layer has a thickness of 103 nm with no additive content, and the solvent vapor annealing time is 5 min. Figure 4a represents the chemical structures of different materials of D16, D18, and Y6. To investigate the absorption of light and photovoltaic parameter output more thoroughly, the researchers measured the absorption spectra for D18 in chloroform and as film in Figure 4b. Generally, D18 shows an absorption band at 400–620 nm. The light absorption peaks at 586 nm for D18 film, corresponding to an energy gap (E_g) of 1.98 eV. The absorption spectra of the Y6 film are complementary to those of D18. Cyclic voltammetry (CV) measurements were used to determine D18's HOMO and LUMO energy levels, which are −5.51 eV and −2.77 eV, respectively, while Y6 shows a HOMO of −5.65 eV and a LUMO of −4.10 eV (see in Figure 4c). The external quantum efficiency (EQE) spectrum for D18 at 460–740 nm is higher than 80%, with a maximum of 87% at 540 nm, which leads to effective photocurrent creation [27].

Another work by Zhu et al. [25] conducted in 2021 shows that a binary OSC based on PBQ6:Y6 achieved a high PCE of 17.62%. The absorption of PBQ6 peaks at 634 nm with an absorption band of 300–750 nm, which is significantly wider than that of D18. The HOMO and LUMO energy levels of PBQ6 are −5.64 eV and −3.18 eV, respectively, while Y6 shows a HOMO of −5.72 eV and a LUMO of −4.06 eV. In comparison with D18 and PBQ6, Y6 has a narrower band gap. The EQE spectra indicate that the device shows a strong photo response on the visible wavelength range of 430–830 nm, and the maximum value of EQE surpassed 85%, with an even stronger photo response in the wavelength range of 600–800 nm. Compared to the D18:Y6 structure, the PBQ6:Y6 structure has a significantly broader EQE spectrum due to large band gaps in the energy diagram. The photo-CELIV measurement indicates that the D18:Y6 structure shows a carrier extraction mobility of 1.59×10^{-3} cm^2 V^{-1}s^{-1}, and the PBQ6:Y6 structure shows a carrier extraction mobility of 1.43×10^{-4} cm^2 V^{-1} s^{-1}. The PCE of the best D18:Y6 cells was 18.22%, with a V_{oc} of 0.859 V, a J_{sc} of 27.70 mA cm^{-2} and an FF of 76.6%. The PBQ6:Y6 based devices demonstrated a PCE of 17.62%, with a V_{oc} of 0.851 V and a J_{sc} of 26.58 mA cm^{-2} and an excellent FF of 77.91%. The reported PCE was the highest among the OSCs, using quinoxaline-based polymers as donors. Compared to the PBQ6:Y6 based devices, the D18:Y6 based device has a lower value in FF but higher values in J_{sc} and V_{oc} due to its high carrier mobility and reduced charge recombination. Another electron donor material with high performance is PBDB-T-2F. Lin et al. [28] investigated the binary cells with the blend of PBDB-T-2F: Y6 as the active layer and showed a PCE of 15.30%, a V_{oc} of 0.850 V, a J_{sc} of

25.02 mA cm^{-2}, and an FF of 72.0% for the investigated cells. The V_{oc} value is significantly approaching those of the two studies mentioned above, but the values of J_{sc} and FF are significantly lower. This is due to the decreased material crystallinity and increased charge recombination in the active layer of PBDB-T-2F: Y6.
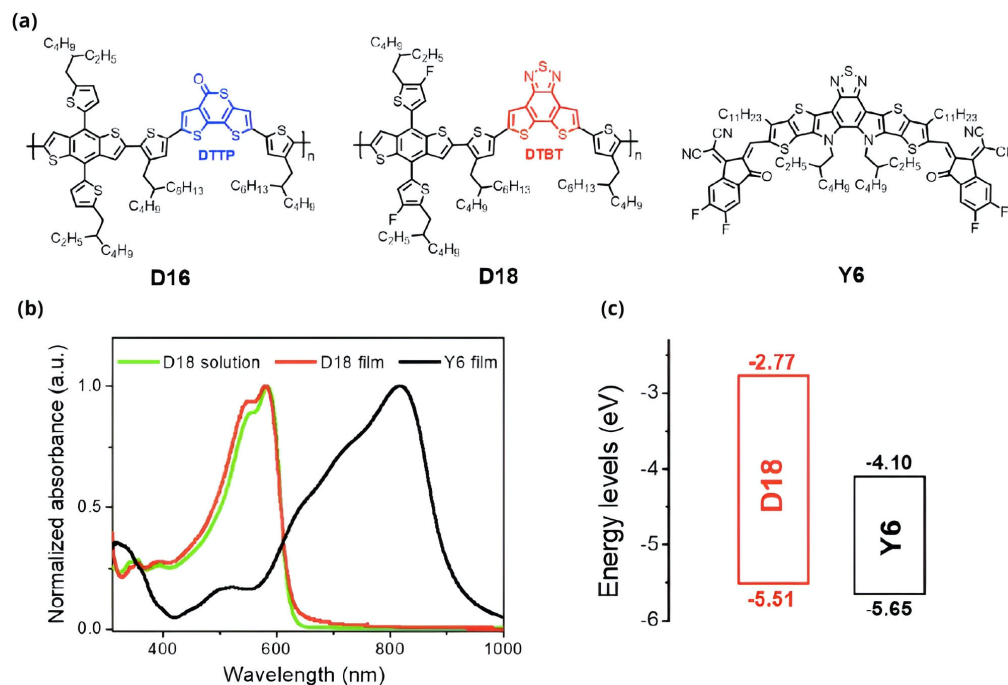

Figure 4. (**a**) The chemical structures of D16, D18, and Y6; (**b**) The absorption bands of D18 solution, D18 film, and Y6 film; and (**c**) The energy band layouts for D18 and Y6. (Reprint with permission from [27]. 2023, Elsevier).

In summary, to improve the next generation of OSC technology, it is important to focus on making changes to the material structure, particularly via alkyl chain modification. Additionally, optimizing the wide band gap donors and non-fullerene acceptors, which should have high solubility and aggregation properties, can improve the material's morphology and crystallinity properties, leading to the creation of more excitons.

2.2. Ternary OSC Structure

Ternary blending in the active layers has proven to be a viable method for achieving high OSC efficiency [27,30,37]. In 2020, Ma et al. [29] fabricated the ternary devices with PM6 as the donor material and Y6 and C8-DTC as the acceptor materials (see their chemical structures in Figure 5a). Ternary OSCs featuring PM6: Y6: C8-DTC have a PCE of 17.52%, with a V_{oc} of 0.873V, a J_{sc} of 26.50 mA cm^{-2} and an FF of 75.61%. In comparison with the previous work on a binary structure (PM6: Y6) with a PCE of 17.23% [22], the study by Ma et al. [29] suggests that the third component (C8-DTC) enhances the PCE. Figure 5c depicts the UV-Vis absorption band of the three photovoltaic materials employed in the ternary OSCs. Y6 shows an absorption band between 700 nm and 950 nm with a peak at 840 nm; PM6 displays an absorption band of 400–700 nm with an absorption peak at 600 nm; C8-DTC demonstrates a narrow absorption band between 600 nm and 800 nm, with an absorption maximum at 730 nm. Therefore, combining these three materials results in complementary absorption across a wide wavelength range of 300 to 1000 nm. The HOMO and LUMO levels of C8-DTC were measured to be −5.60 eV and −3.87 eV, respectively. The comparison between Y6 and C8-DTC shows that C8-DTC has a higher LUMO level, as shown in Figure 5b, which is helpful for the increments of V_{oc} in the ternary OSCs. The C8-DTC energy levels create an energy cascade with the HOMO and LUMO levels of PM6 and Y6; this is essential for the enhanced electron transport in ternary OSCs

due to the approaching HOMO and LUMO energy levels [29]. To determine the impact of C8-DTC on the charge transport parameters of ternary OSCs, it is necessary to to analyze the mobilities of charge carriers (e.g., holes and electrons). The study of the binary structure (PM6:Y6) [22] shows that the electron mobilities (μ_e) and hole mobilities (μ_h) of the binary blend are 3.84×10^{-4} cm^2 V^{-1} s^{-1} and 1.66×10^{-4} cm^2 V^{-1}s^{-1}, respectively, with a μ_e/μ_h ratio of 2.34. The study of the ternary structure (PM6:Y6:C8-DTC with a weight ratio of 1:1.08:0.12) [29] shows that μ_e and μ_h of the ternary blend are 4.45×10^{-4} cm^2 V^{-1} s^{-1} and 2.42×10^{-4} cm^2 V^{-1} s^{-1}, respectively, with a μ_e/μ_h ratio of 1.8. This demonstrates that the μ_e and μ_h values of the ternary blend are greater than those of the binary blend, thereby leading to the enhancement of FF and J_{sc} values of the ternary OSCs.
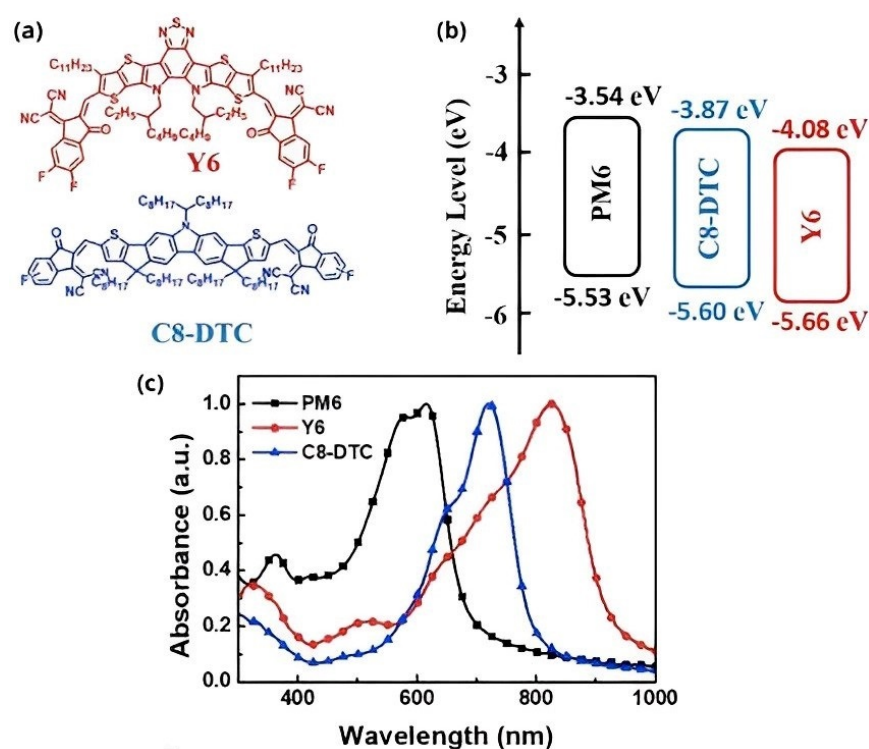

Figure 5. (**a**) Chemical structures of Y6 and C8−DTC; (**b**) The energy level diagrams of PM6, Y6, and C8−DTC; (**c**) Absorption spectra of PM6, Y6 and C8−DTC films. (Reprint with permission from [29]. 2023, Elsevier).

The superior performance of ternary cells over conventional binary cells is also partially due to the improved morphology of the active layer. The ideal binary blend films of PM6: Y6 have a surface roughness of 1.704 nm. As shown in Figure 6, the ternary blend film of PM6: Y6: C8-DTC has a lower surface roughness value of 1.246 nm. Adding C8-DTC to the PM6: Y6 system generates a nanoscale phase separation network morphology, which promotes charge carrier transfer and charge separation in the active layer.

Lin et al. [28] presented another structure of ternary OSCs, namely, PBDB-T-2F:Y6:PC71BM. The EQE spectra for the ternary PBDB-T-2F:Y6:PC71BM cells show a high EQE beyond 600 nm. Moreover, the average internal quantum efficiency (IQE) of OSCs in the wavelength range of 350–850 nm is equal to 91.7% and presents high absorbance at the 600 nm wavelength due to the complexity of the energy levels of the three materials. The device yields a PCE of 17% with a V_{oc} of 0.84 V, a J_{sc} of 26.0 mA cm^{-2} and an enhanced FF of 78%. Ram et al. [24] designed a similar structure but replaced Lin et al.'s [28] PC$_{71}$BM with non-fullerene SF(BR)$_4$ and incorporated moth eye anti-reflecting coating on top of the glass. The modified structure of the ternary OSC in this study is moth-eye ARC/glass/ITO/WS2/PBDB-T-2F: Y6: SF (BR)$_4$/PFN-Br/Al, which yielded a PCE of 20.87%, the highest ever PCE for ternary OSCs to date. Comparison of the energy levels

of two materials (SF(BR)$_4$ and PC$_{71}$BM) in Figure 7 reveals that the LUMO and HOMO energy levels of SF (BR)$_4$ are −5.78 eV and −3.73 eV, respectively; the LUMO and HOMO energy levels of PC$_{71}$BM are −6.1 and −3.8 eV, respectively. It is clear that the energy levels of SF(BR)$_4$ are much closer to the LUMO and HOMO levels of PBDB-T-2F and Y6 than those of PC$_{71}$BM. This means that SF(BR)$_4$ shows a higher absorbance rate and better complementarity with the other two materials than PC$_{71}$BM.
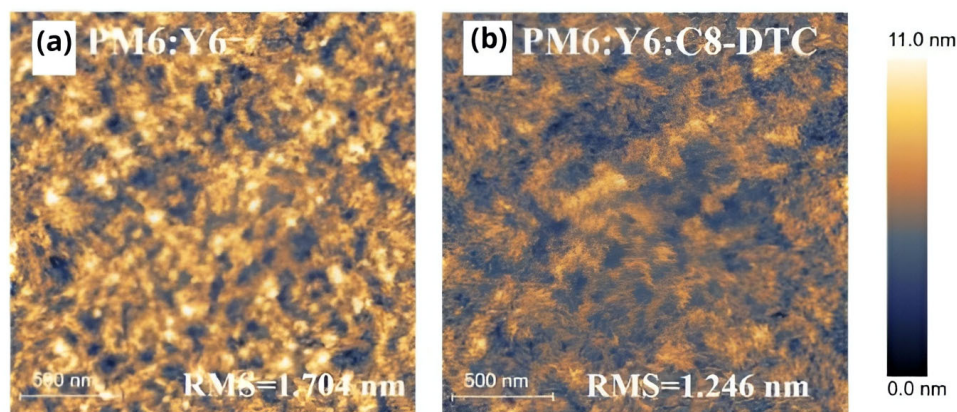

Figure 6. AFM images of (**a**) binary PM6: Y6 and (**b**) ternary PM6: Y6: C8−DTC blend films. (Reprint with permission from [29]. 2023, Elsevier).
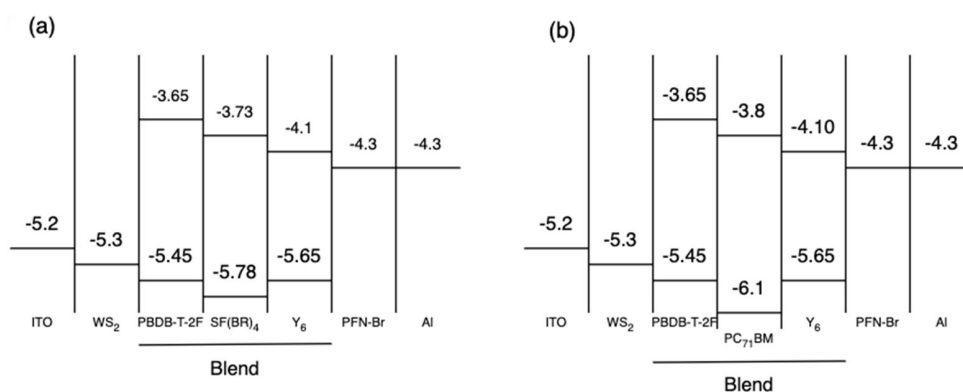

Figure 7. (**a**) Energy level diagram (energies are in eV) for BHJ based ternary OSCs with the cell structure of moth−eye AR/glass/ITO/WS2/PBDB−T−2F:Y6:SF(BR)4/PFN−Br/Al; (**b**) Energy level diagram (energies are in eV) for BHJ based ternary OSC with the cell structure of glass/ITO/WS2/PBDB−T−2F:Y6:PC71BM/PFN−Br/Al. (Reprint with permission from [24]. 2022, Wiley).

In summary, ternary solar cells have greatly interested the organic photovoltaics community. The relevance of the third component in ternary OSCs is that it creates a broad and complementary light absorption band in the active layer and also forms an energy cascade between the energy levels (LUMO and HOMO) of the materials in the active layer, thereby facilitating the charge transport and leading to the enhancement of FF, V_{oc}. and PCE. By selecting the photoactive layer's three components with care, all photovoltaic characteristics can be simultaneously improved in ternary solar cells. Furthermore, the material surface in the ternary solar cells has reduced roughness, which can result in higher solubility and aggregation properties for enhancing cell performance.

2.3. Interface Engineering

In OSCs, interfacial materials also play essential roles alongside the active layer to enhance the PCE of the device. In 2019, Lin et al. [28] reported OSCs with the ternary BHJ (PBDBT-2F:Y6:PC71BM) and the HTL (PEDOT:PSS) and obtained a PCE of 16.4%, an

FF of 78%, a V_{oc} of 0.84 V, and a J_{sc} of 26 mA cm^2. Under the same conditions, replacing PEDOT:PSS with WS2 as the HTL results in an augmentation of PCE to 17%, which is due to the highly conductive WS2. Measurement of the serial resistances (R_s) of the two devices indicates that the PEDOT:PSS based device shows higher R_s than the WS2 based device, which is due to the efficient charge transport and low resistance in the WS2 HTL [28]. In 2020, Zhang et al. [21] used an aliphatic amine group functionalized PDI derivative (PDINN) and stable metals (silver and copper) in the air as the cathode interlayer material (CIM) and the top cathode of an OSC, respectively. PDINN is relatively cheap and can be easily synthesized in a laboratory. The existence of the aliphatic amine group ensures an excellent connection between the top cathode and the active layer. The PDINN contacts NFA-based active layers tightly and shows superior electric conduction (5.0×10^{-4} S cm^{-1}) and charge collection abilities. Furthermore, OSCs based on PDINN show weak dependence on the change of PDINN thickness during device manufacturing, since the device PCE remains above 15.0% as the thickness of PDINN expands to 27 nm. If the same active layer (PM6:Y6) was utilized in the preparation of OSCs, the PDINO/Ag based device achieves a PCE of 15.17%, a V_{oc} of 0.821 V, a J_{sc} of 25.58 mA cm^{-2} and an FF of 72.24%, while the PDINN/Ag based device achieves a higher PCE of 17.23%. The remarkable efficiency enhancement for PDINN/Ag-based devices can be attributed to the increment of V_{oc} from 0.821 to 0.847 V, and FF from 72.24% to 78.59% [38]. These results suggest that regulating interfacial contacts with proper intermolecular modifications could enhance the performance of OSC devices.

3. Conclusions

This mini-review gives an overview of the most recent developments in single-junction OSCs with high PCE. It shows that OSCs with PCEs above 20% have been made by combining different strategies, such as new non-fullerene electron acceptors with high absorption in the solar spectrum, minimal loss in the driving force during charge separation, film shape, interfacial layer, and device engineering. The most advanced result of PCE has achieved a high value of 20.87% in ternary OCSs, which feature the addition of a third component in the active layer in comparison with the binary OSCs. The third component contributes to improvements in the energy level cascade and charge transport between the device's layers, which jointly result in a PCE higher than the binary OSCs. As seen in the reviewed studies, the binary and ternary BHJ OSCs have a significant advantage over inorganic solar cells in terms of their flexibility, low fabrication cost, less pollution, and a short energy pack-back time. Currently, OSCs exhibit lower PCE and stability compared to their inorganic counterparts. However, due to the intense research efforts being devoted to OSCs, there is an opportunity to overcome these challenges and improve their PCE and stability.

For better development of the next-generation OSC technology, future investigations may focus more on modifying the structures of active materials with alkyl chains, synthesizing new donors and acceptors with high solubility and aggregation properties to create more excitons, and optimizing the ternary structure to overcome the problems that undermine the efficiency of binary OSCs.

Author Contributions: Conceptualization, B.M.E.A.; methodology, B.M.E.A.; formal analysis, B.M.E.A., Y.Z. and H.L.; investigation, B.M.E.A., Y.Z. and H.L.; resources, Q.W., J.X. and C.Z.; data curation, B.M.E.A. and C.Z.; writing—original draft preparation, B.M.E.A.; writing—review and editing, B.M.E.A. and C.Z.; supervision, J.X. and C.Z.; project administration, B.M.E.A. and C.Z.; funding acquisition, C.Z. All authors have read and agreed to the published version of the manuscript.

Data Availability Statement: Not applicable.

Conflicts of Interest: The authors declare no conflict of interest.

References

1. McDowell, C.; Bazan, G.C. Organic solar cells processed from green solvents. *Curr. Opin. Green Sustain. Chem.* **2017**, *5*, 49–54. [CrossRef]
2. Luo, G.; Wu, H. Organic solar cells: Going green. *Nat. Energy* **2016**, *1*, 16001. [CrossRef]
3. Tian, X.; Stranks, S.D.; You, F. Life cycle energy use and environmental implications of high-performance perovskite tandem solar cells. *Sci. Adv.* **2020**, *6*, eabb0055. [CrossRef]
4. Ithikkal, J.P.; Yabara, Y.; Uto, S.; Izawa, S.; Hiramoto, M. Lateral-tandem organic photovoltaic cells with carrier transport and generation layers. *Appl. Phys. Express* **2021**, *14*, 101003. [CrossRef]
5. Niederhausen, J.; Mazzio, K.A.; MacQueen, R.W. Inorganic–organic interfaces in hybrid solar cells. *Electron. Struct.* **2021**, *3*, 033002. [CrossRef]
6. Rhaman, M.M.; Matin, M.A. Organic Solar Cells: Historical developments and challenges. In Proceedings of the 2015 International Conference on Advances in Electrical Engineering (ICAEE), Dhaka, Bangladesh, 17–19 December 2015; pp. 26–29. [CrossRef]
7. Salikhov, R.B.; Biglova, Y.N.; Mustafin, A.G. New organic polymers for solar cells. In *Emerging Solar Energy Materials*; Ameen, S., Akhtar, M.S., Shin, H.-S., Eds.; IntechOpen: Rijeka, Croatia, 2018. [CrossRef]
8. Scharber, M.C.; Sariciftci, N.S. Efficiency of bulk-heterojunction organic solar cells. *Prog. Polym. Sci.* **2013**, *38*, 1929–1940. [CrossRef]
9. Chen, L.-M.; Hong, Z.; Li, G.; Yang, Y. Recent Progress in Polymer Solar Cells: Manipulation of Polymer: Fullerene Morphology and the Formation of Efficient Inverted Polymer Solar Cells. *Adv. Mater.* **2009**, *21*, 1434–1449. [CrossRef]
10. Burke, D.J.; Lipomi, D.J. Green chemistry for organic solar cells. *Energy Environ. Sci.* **2013**, *6*, 2053–2066. [CrossRef]
11. Bagher, A.M. Comparison of Organic Solar Cells and Inorganic Solar Cells. *Int. J. Renew. Sustain. Energy* **2014**, *3*, 53–58. [CrossRef]
12. Wibowo, F.T.A.; Krishna, N.V.; Sinaga, S.; Lee, S.; Hadmojo, W.T.; Do, Y.R.; Jang, S.-Y. High-efficiency organic solar cells prepared using a halogen-free solution process. *Cell Rep. Phys. Sci.* **2021**, *2*, 100517. [CrossRef]
13. Tadeson, G.; Sabat, R.G. Enhancement of the Power Conversion Efficiency of Organic Solar Cells by Surface Patterning of Azobenzene Thin Films. *ACS Omega* **2019**, *4*, 21862–21872. [CrossRef] [PubMed]
14. Bonasera, A.; Giuliano, G.; Arrabito, G.; Pignataro, B. Tackling Performance Challenges in Organic Photovoltaics: An Overview about Compatibilizers. *Molecules* **2020**, *25*, 2200. [CrossRef]
15. Wang, G.; Melkonyan, F.S.; Facchetti, A.; Marks, T.J. All-Polymer Solar Cells: Recent Progress, Challenges, and Prospects. *Angew. Chem. Int. Ed.* **2019**, *58*, 4129–4142. [CrossRef] [PubMed]
16. Rafique, S.; Abdullah, S.M.; Sulaiman, K.; Iwamoto, M. Fundamentals of bulk heterojunction organic solar cells: An overview of stability/degradation issues and strategies for improvement. *Renew. Sustain. Energy Rev.* **2018**, *84*, 43–53. [CrossRef]
17. Xu, X.; Yu, L.; Meng, H.; Dai, L.; Yan, H.; Li, R.; Peng, Q. Polymer Solar Cells with 18.74% Efficiency: From Bulk Heterojunction to Interdigitated Bulk Heterojunction. *Adv. Funct. Mater.* **2022**, *32*, 2108797. [CrossRef]
18. Chen, L.X. Organic Solar Cells: Recent Progress and Challenges. *ACS Energy Lett.* **2019**, *4*, 2537–2539. [CrossRef]
19. Lai, T.-H.; Tsang, S.W.; Manders, J.R.; Chen, S.; So, F. Properties of interlayer for organic photovoltaics. *Mater. Today* **2013**, *16*, 424–432. [CrossRef]
20. Cui, Y.; Yao, H.; Hong, L.; Zhang, T.; Tang, Y.; Lin, B.; Xian, K.; Gao, B.; An, C.; Bi, P.; et al. Organic photovoltaic cell with 17% efficiency and superior processability. *Natl. Sci. Rev.* **2020**, *7*, 1239–1246. [CrossRef] [PubMed]
21. Zhang, M.; Zhu, L.; Zhou, G.; Hao, T.; Qiu, C.; Zhao, Z.; Hu, Q.; Larson, B.W.; Zhu, H.; Ma, Z.; et al. Single-layered organic photovoltaics with double cascading charge transport pathways: 18% efficiencies. *Nat. Commun.* **2021**, *12*, 309. [CrossRef] [PubMed]
22. Yao, J.; Qiu, B.; Zhang, Z.-G.; Xue, L.; Wang, R.; Zhang, C.; Chen, S.; Zhou, Q.; Sun, C.; Yang, C.; et al. Cathode engineering with perylene-diimide interlayer enabling over 17% efficiency single-junction organic solar cells. *Nat. Commun.* **2020**, *11*, 2726. [CrossRef]
23. Cui, Y.; Xu, Y.; Yao, H.; Bi, P.; Hong, L.; Zhang, J.; Zu, Y.; Zhang, T.; Qin, J.; Ren, J.; et al. Single-Junction Organic Photovoltaic Cell with 19% Efficiency. *Adv. Mater.* **2021**, *33*, 2102420. [CrossRef] [PubMed]
24. Ram, K.S.; Singh, J. Over 20% Efficient and Stable Non-Fullerene-Based Ternary Bulk-Heterojunction Organic Solar Cell with WS 2 Hole-Transport Layer and Graded Refractive Index Antireflection Coating. *Adv. Theory Simul.* **2020**, *3*, 2000047. [CrossRef]
25. Zhu, C.; Meng, L.; Zhang, J.; Qin, S.; Lai, W.; Qiu, B.; Yuan, J.; Wan, Y.; Huang, W.; Li, Y. A Quinoxaline-Based D–A Copolymer Donor Achieving 17.62% Efficiency of Organic Solar Cells. *Adv. Mater.* **2021**, *33*, 2100474. [CrossRef]
26. Cui, Y.; Yao, H.; Zhang, J.; Xian, K.; Zhang, T.; Hong, L.; Wang, Y.; Xu, Y.; Ma, K.; An, C.; et al. Single-Junction Organic Photovoltaic Cells with Approaching 18% Efficiency. *Adv. Mater.* **2020**, *32*, 1908205. [CrossRef] [PubMed]
27. Liu, Q.; Jiang, Y.; Jin, K.; Qin, J.; Xu, J.; Li, W.; Xiong, J.; Liu, J.; Xiao, Z.; Sun, K.; et al. 18% Efficiency organic solar cells. *Sci. Bull.* **2020**, *65*, 272–275. [CrossRef] [PubMed]
28. Lin, Y.; Adilbekova, B.; Firdaus, Y.; Yengel, E.; Faber, H.; Sajjad, M.; Zheng, X.; Yarali, E.; Seitkhan, A.; Bakr, O.M.; et al. 17% Efficient Organic Solar Cells Based on Liquid Exfoliated WS₂ as a Replacement for PEDOT:PSS. *Adv. Mater.* **2019**, *31*, 1902965. [CrossRef] [PubMed]
29. Ma, Q.; Jia, Z.; Meng, L.; Zhang, J.; Zhang, H.; Huang, W.; Yuan, J.; Gao, F.; Wan, Y.; Zhang, Z.; et al. Promoting charge separation resulting in ternary organic solar cells efficiency over 17.5%. *Nano Energy* **2020**, *78*, 105272. [CrossRef]

30. Lin, Y.; Nugraha, M.I.; Firdaus, Y.; Scaccabarozzi, A.D.; Aniés, F.; Emwas, A.-H.; Yengel, E.; Zheng, X.; Liu, J.; Wahyudi, W.; et al. A Simple n-Dopant Derived from Diquat Boosts the Efficiency of Organic Solar Cells to 18.3%. *ACS Energy Lett.* **2020**, *5*, 3663–3671. [CrossRef]

31. Lin, Y.; Firdaus, Y.; Nugraha, M.I.; Liu, F.; Karuthedath, S.; Emwas, A.; Zhang, W.; Seitkhan, A.; Neophytou, M.; Faber, H.; et al. 17.1% Efficient Single-Junction Organic Solar Cells Enabled by n-Type Doping of the Bulk-Heterojunction. *Adv. Sci.* **2020**, *7*, 1903419. [CrossRef]

32. Gusain, A.; Faria, R.M.; Miranda, P.B. Polymer Solar Cells—Interfacial Processes Related to Performance Issues. *Front. Chem.* **2019**, *7*, 61. [CrossRef]

33. Narayan, M.; Singh, J. Photovoltaic contribution of photo-generated excitons in acceptor material of organic solar cells. *J. Mater. Sci. Mater. Electron.* **2017**, *28*, 7070–7076. [CrossRef]

34. Singh, J.; Narayan, M.; Ompong, D.; Zhu, F. Dissociation of charge transfer excitons at the donor–acceptor interface in bulk heterojunction organic solar cells. *J. Mater. Sci. Mater. Electron.* **2017**, *28*, 7095–7099. [CrossRef]

35. An, Q.; Zhang, F.; Zhang, J.; Tang, W.; Deng, Z.; Hu, B. Versatile ternary organic solar cells: A critical review. *Energy Environ. Sci.* **2016**, *9*, 281–322. [CrossRef]

36. Lee, J.-H.; Takafuji, M.; Sagawa, T.; Ihara, H. Reappraising the validity of poly(3-hexylthiophene) nanostructures in interdigitated bilayer organic solar cells. *Sol. Energy Mater. Sol. Cells* **2016**, *147*, 68–74. [CrossRef]

37. Gillett, A.J.; Privitera, A.; Dilmurat, R.; Karki, A.; Qian, D.; Pershin, A.; Londi, G.; Myers, W.K.; Lee, J.; Yuan, J.; et al. The role of charge recombination to triplet excitons in organic solar cells. *Nature* **2021**, *597*, 666–671. [CrossRef]

38. Wang, X.; Sun, Q.; Gao, J.; Wang, J.; Xu, C.; Ma, X.; Zhang, F. Recent Progress of Organic Photovoltaics with Efficiency over 17%. *Energies* **2021**, *14*, 4200. [CrossRef]

39. Trindade, A.J.; Pereira, L. Bulk Heterojunction Organic Solar Cell Area-Dependent Parameter Fluctuation. *Int. J. Photoenergy* **2017**, *2017*, 1364152. [CrossRef]

40. Hafeez, H.Y.; Iro, Z.S.; Saadu, I.; Adam, B.I. Fabrication and Characterization of Silicon-Based Solar Cell Using Keithley 2400 SMU. *IOSR J. Appl. Phys.* **2016**, *8*, 17–21. [CrossRef]

41. Felekidis, N.; Melianas, A.; Kemerink, M. Design Rule for Improved Open-Circuit Voltage in Binary and Ternary Organic Solar Cells. *ACS Appl. Mater. Interfaces* **2017**, *9*, 37070–37077. [CrossRef]

42. Zhang, F.; Inganäs, O.; Zhou, Y.; Vandewal, K. Development of polymer–fullerene solar cells. *Natl. Sci. Rev.* **2016**, *3*, 222–239. [CrossRef]

43. Würfel, P. Photovoltaic Principles and Organic Solar Cells. *Chimia* **2007**, *61*, 770. [CrossRef]